Pucella, G; Alessi, E.; Amicucci, L.; Angelini, B.; Apicella, M.L.; Apruzzese, G.; Artaserse, G.; Belli, F.; Bin, W.; Boncagni, L., et al. (2017). Overview of the FTU results. *Nuclear Fusion*, 57(10), 102004, [12] p.

DOI: https://doi.org/10.1088/1741-4326/aa6239

Overview of the FTU results

G. Pucella[1], E. Alessi[2], L. Amicucci[1], B. Angelini[1], M.L. Apicella[1], G. Apruzzese[1], G. Artaserse[1], F. Belli[1], W. Bin[2], L. Boncagni[1], A. Botrugno[1], S. Briguglio[1], A. Bruschi[2], P. Buratti[1], G. Calabrò[1], M. Cappelli[1], A. Cardinali[1], C. Castaldo[1], F. Causa[1], S. Ceccuzzi[1], C. Centioli[1], R. Cesario[1], C. Cianfarani[1], G. Claps[1], V. Cocilovo[1], F. Cordella[1], F. Crisanti[1], O. D'Arcangelo[1], M. De Angeli[2], C. Di Troia[1], B. Esposito[1], D. Farina[2], L. Figini[2], G. Fogaccia[1], D. Frigione[1], V. Fusco[1], L. Gabellieri[1], S. Garavaglia[2], E. Giovannozzi[1], G. Granucci[2], M. Iafrati[1], F. Iannone[1], M. Lontano[2], G. Maddaluno[1], S. Magagnino[1], M. Marinucci[1], D. Marocco[1], G. Mazzitelli[1], C. Mazzotta[1], A. Milovanov[1], D. Minelli[2], F.C. Mirizzi[3], A. Moro[2], S. Nowak[2], D. Pacella[1], L. Panaccione[3], M. Panella[3], V. Pericoli-Ridolfini[3], A. Pizzuto[1], S. Podda[1], G. Ramogida[1], G. Ravera[1], D. Ricci[2], A. Romano[1], C. Sozzi[2], A.A. Tuccillo[1], O. Tudisco[1], B. Viola[1], V. Vitale[1], G. Vlad[1], M. Zerbini[1], F. Zonca[1], M. Aquilini[1], P. Cefali[1], E. Di Ferdinando[1], S. Di Giovenale[1], G. Giacomi[1], A. Grosso[1], V. Mellera[2], M. Mezzacappa[1], A. Pensa[1], P. Petrolini[1], V. Piergotti[1], B. Raspante[1], G. Rocchi[1], A. Sibio[1], B. Tilia[1], R. Tulli[1], M. Vellucci[1], D. Zannetti[1], I. Bogdanovic-Radovic[4], D. Carnevale[5], A. Casolari[6], M. Ciotti[1], C. Conti[7], P.P. Dinca[8], V. Dolci[1], C. Galperti[9], M. Gospodarczyk[5], G. Grosso[2], L. Lubiako[10], M. Lungu[8], J.R. Martin-Solis[11], C. Meineri[1], F. Murtas[12], A. Nardone[2], F.P. Orsitto[3], E. Perelli Cippo[2], Z. Popovic[11], D. Ripamonti[13], A. Simonetto[2] and U. Tartari[2]

[1] ENEA, Fusion and Nuclear Safety Department, C. R. Frascati, Via E. Fermi 45, 00044 Frascati (Roma), Italy
[2] IFP-CNR, Istituto di Fisica del Plasma, Via R. Cozzi 53, 20125 Milano, Italy
[3] Consorzio CREATE, Università di Napoli Federico II, Via Claudio 21, 80125 Napoli, Italy
[4] Ruder Boskovic Institute, Bijenicka Cesta 54, 10000 Zagreb, Croatia
[5] Dipartimento di Ingegneria Civile e Ingegneria Informatica, Università di Roma Tor Vergata, Viale del Policlinico 1, 00133 Roma, Italy
[6] Dipartimento di Fisica, Università di Pisa, Largo B. Pontecorvo 3, 56127 Pisa, Italy
[7] ICVBC-CNR, Istituto per la Conservazione e la Valorizzazione dei Beni Culturali, Via R. Cozzi 53, 20125 Milano, Italy
[8] National Institute for Laser, Plasma and Radiation Physics, 077125 Magurele (Bucharest), Romania
[9] École Polytechnique Fédérale de Lausanne, CRPP, Route Cantonale, 1015 Lausanne, Switzerland
[10] Institute of Applied Physics of Russian Academy of Sciences, Nizhny Novgorod, Russia
[11] Universidad Carlos III de Madrid, Avenida de la Universidad 30, 28911 Madrid, Spain
[12] Istituto Nazionale di Fisica Nucleare, Via E. Fermi 40, 00044 Frascati (Roma), Italy
[13] ICMATE-CNR, Istituto di Chimica della Materia Condensata e di Tecnologie per l'Energia, Via R. Cozzi 53, 20125 Milano, Italy

E-mail: gianluca.pucella@enea.it

Abstract

Experiments on runaway electrons have been performed for the determination of the critical electric field for runaway generation. A large database of post-disruption runaway beams has been analyzed in order to identify linear dynamical models for new position and current runaway beam controllers, and experiments of electron cyclotron assisted plasma start-up have shown the presence of runaway electrons also below the expected electric field threshold,

indicating that the radio-frequency power acts as seeding for fast electrons. A linear micro-stability analysis of neon-doped pulses has been carried out to investigate the mechanisms leading to the observed density peaking. A study of the ion drift effects on the MARFE instability has been performed and the peaking of density profile in the high density regime has been well reproduced using a thermo-diffusive pinch in the particle transport equation. The study of the density limit performed in the past has been extended towards lower values of toroidal magnetic field and plasma current. The analysis of the linear stability of the 2/1 tearing mode observed in high density plasmas has highlighted a destabilization with increasing peaking of the current profile during the density ramp-up, while the final phase of the mode temporal evolution is characterized by limit cycles on the amplitude/frequency plane. A liquid lithium limiter with thermal load capability up to 10 MW m^{-2} has been tested. The pulse duration has been extended up to 4.5 s and elongated configurations have been obtained for 3.5 s, with the X-point just outside the plasma chamber. A W/Fe sample has been exposed in the scrape-off layer in order to study the sputtering of Fe and the W enrichment of the surface layer. Dusts have been collected and analyzed, showing that the metallic population exhibits a high fraction of magnetic grains. A new diagnostic for in-flight runaway electron studies has allowed the image and the visible/infrared spectrum of the forward and backward synchrotron radiation to be provided simultaneously. A fast infrared camera for thermo-graphic analysis has provided the pattern of the toroidal limiter heating by disruption heat loads, and a triple-GEM detector has been tested for soft x-ray diagnostics. The collective Thomson scattering diagnostic has been upgraded and used for investigations on parametric decay instability excitation by electron cyclotron beams correlated with magnetic islands, and new capabilities of the Cherenkov probe have been explored in the presence of beta-induced Alfvén eigenmodes associated to high amplitude magnetic islands.

Keywords: tokamak, overview, FTU

1. Introduction

FTU is a compact high magnetic field machine (toroidal magnetic field B_T up to 8 T, plasma current I_p up to 1.6 MA) with circular poloidal cross-section (major radius $R_0 = 0.935$ m, minor radius $a = 0.30$ m) and metallic first wall (figure 1). The stainless steel vacuum chamber is covered internally, at the high field side, by a toroidal limiter made of molybdenum tiles, and a molybdenum poloidal limiter is also present at the low field side. Additional heating systems are available, namely a 140 GHz electron cyclotron system with power up to 1.5 MW and a 8.0 GHz lower hybrid system with power up to 2.0 MW [1]. Since the *2014 IAEA Fusion Energy Conference* in St. Petersburg, FTU operations were devoted to experiments on runaway electron generation and control, MHD instabilities in the high density regime, transport properties in neon-doped pulses and in the presence of MARFE instability, dust analysis, and investigations about the plasma-facing components. New diagnostics, such as a visible/infrared detector for in-flight runaway studies, a fast infrared camera for thermo-graphic analysis of plasma-facing components and a triple-GEM detector for soft x-rays diagnostic, were successfully installed and tested, and new capabilities of the collective Thomson scattering diagnostic and of the Cherenkov probe were explored.

2. Runaway electrons (RE)

2.1. Runaway electrons onset and suppression

Experiments of RE onset and suppression during the flat-top phase of ohmic pulses in FTU [2, 3], leading to the addition of new data points to the existing database on the critical electric field for RE generation (E_{thr}), have confirmed that the measured E_{thr} is $2 \div 5$ times larger than predicted by the relativistic collisional theory (E_R) [4, 5]:

$$E_R = \frac{n_e e^3 \ln \Lambda}{4\pi\epsilon_0^2 m_e c^2} \tag{1}$$

and it is consistent with the new threshold (E_R^{rad}) calculated including synchrotron radiation losses [6] (figure 2):

$$\frac{E_R^{rad}}{E_R} \cong 1 + C_{(Z_{eff})}\left(\frac{2\epsilon_0 B^2}{3 m_e n_e \ln \Lambda}\right)^{0.45}. \tag{2}$$

The RE onset is obtained through a decreasing electron density in the plasma current flat-top, whilst the RE suppression is achieved by starting a pulse with low gas pre-fill thus creating a RE population subsequently suppressed by a feedback-controlled phase of increasing electron density. The time of RE onset/suppression is determined through the comparison of the time traces of a set of absolutely calibrated neutron detectors (BF3

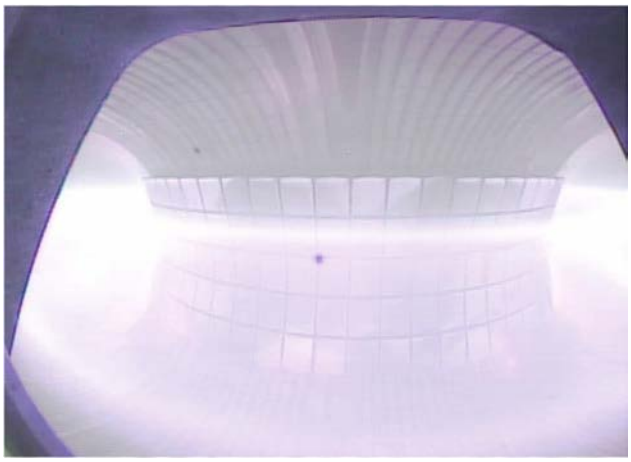

Figure 1. Visible light emission from the plasma torus in the Frascati Tokamak Upgrade (FTU).

chambers) with those of a liquid organic scintillator (NE213), which is sensitive to both neutrons and γ-rays. In the RE onset experiments, during the pre-RE phase the NE213 signal overlaps the BF3 signal, while, as soon as the REs are generated, the two time traces diverge. On the other hand, in the RE suppression experiments, the NE213 signal is higher in the initial phase, indicating the presence of REs, while later on, when RE suppression occurs, the two signals coincide. It is worth noting that the differences observed between E_{thr} for the RE onset and suppression pulses are associated to the methodology used for determining E_{thr} in these experiments. During the RE onset pulses, due to the limited sensitivity of the detectors, some REs may already exist before the BF3 and the NE213 time traces deviate from each other, so that the critical density is underestimated and, hence, the measured E_{thr} at given density is larger than the actual critical field. For the RE suppression experiments, the critical density is reached before the BF3 and NE213 are observed to overlap (some time is required to suppress the REs once the critical conditions are reached). Therefore, the critical density inferred when the two signals overlap is larger than the real one and the measured E_{thr} at given density will be lower than the actual critical field. Hence, the use of the RE onset and suppression experiments provide upper and lower bounds for the critical electric field, respectively [2, 3].

2.2. Runaway beam control

RE beam current ramp-down policies using the central solenoid have been implemented on FTU in order to confirm the possibility of RE beam mitigation without the use of massive gas injection. The control system acts on the central solenoid to induce RE beam current ramp-down meanwhile the beam is kept away from the vessel [7]. The study has revealed that the decay rate during RE beam current ramp-down is a key parameter for runaway current suppression. In particular, small decay rates are less demanding for the radial/vertical stabilization and are therefore better than fast RE current decay, which induce also strong magnetic forces on the mechanical structure.

An example of the effectiveness of the new RE control algorithm for real-time control of post-disruption RE beams is reported in figure 3, where two initially similar pulses are compared, showing that a reduced plasma-facing components interaction is obtained with the new controller active, as evidenced by the reduced fission chamber signal while RE current is ramped-down by induction. Current studies are also devoted to investigate the optimal current decay rate as compared to the measured loop voltage. In fact, experimental findings suggest that post-disruption RE beam suppression is mainly achieved when the decay rate is of about 1 MA s^{-1}, as provided also by other researchers on different tokamaks, such as DIII-D and Tore Supra [8, 9]. A large database (650 pulses) of highly energetic post-disruption RE beams, produced spontaneously or with high-Z gas injection, has been analyzed, in order to identify linear dynamical models. These models [10] have shown a good agreement with experimental data and they are now used to derive new current and position controllers with the goal of providing reliable RE beam suppression strategies.

2.3. Runaway generation during electron cyclotron (EC) assisted plasma start-up

Due to the intrinsic limited toroidal electric field achievable with superconducting poloidal coils, in ITER the start-up phase of plasma current will be obtained with the assistance of EC wave additional power. The FTU tokamak has contributed to this subject together with a group of other tokamaks, by performing experiments focused on low electric field start-up using injection of EC power [11, 12]. Evidence of a potentially dangerous presence of REs at the plasma initiation has been observed in the FTU database of EC assisted plasma start-up experiments, comparing the time traces of the liquid organic scintillator and the set of neutron detectors (figure 4, left side). The results show the generation of REs even at moderate EC power injection (400 kW), in conditions of toroidal electric field E_{Loop} well below the Dreicer field threshold E_{Dreicer} for primary generation, evidencing that EC waves moderately increase the energy of electrons, which may be further accelerated by the toroidal electric field to runaway. The database has been analyzed in order to find a possible parameter controlling RE generation, assuming that the electric field is not the only relevant parameter. The exploration has evidenced a dependency on the pre-filling pressure (figure 4, right side) more than on the plasma density during the EC pulse. It is worth noting that, in the relevant phase for RE formation due to EC power, the density exhibits a strong peaked profile around the EC resonance, so that it can be considered a local parameter, while the pre-filling pressure is a more global quantity. This seems to be the reason why the REs are more influenced by volume distributed neutrals instead of by localized ionized plasma. The same figure seems to indicate lower production of REs in case of injection of wave in XM2 polarization.

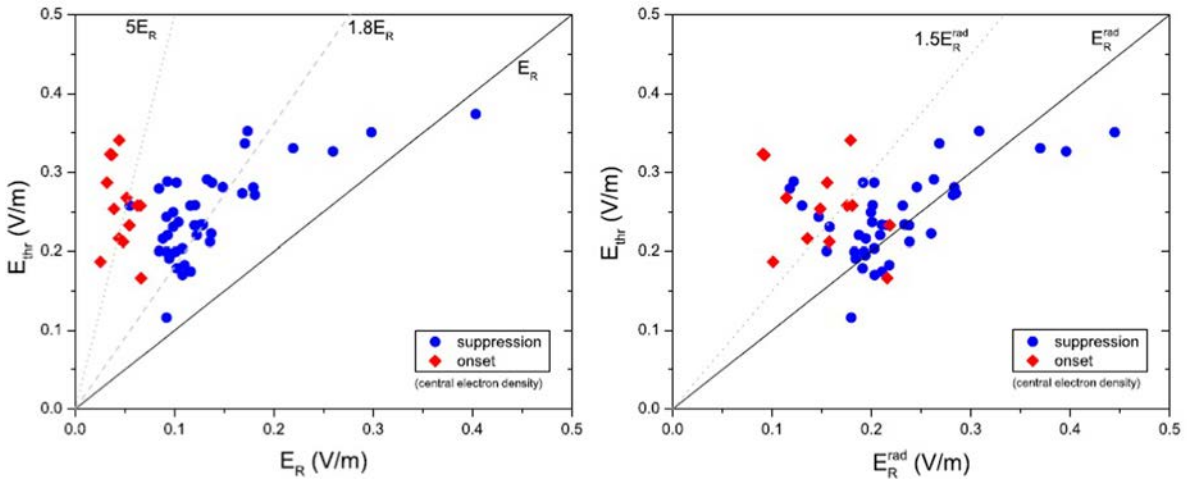

Figure 2. Comparison of measured $E_{\rm thr}$ with relativistic collisional (left) and collisional + synchrotron radiation (right) theory predictions. The predicted electric fields have been evaluated using the local central electron density instead of the line-averaged central density, since REs are initially generated in the plasma core.

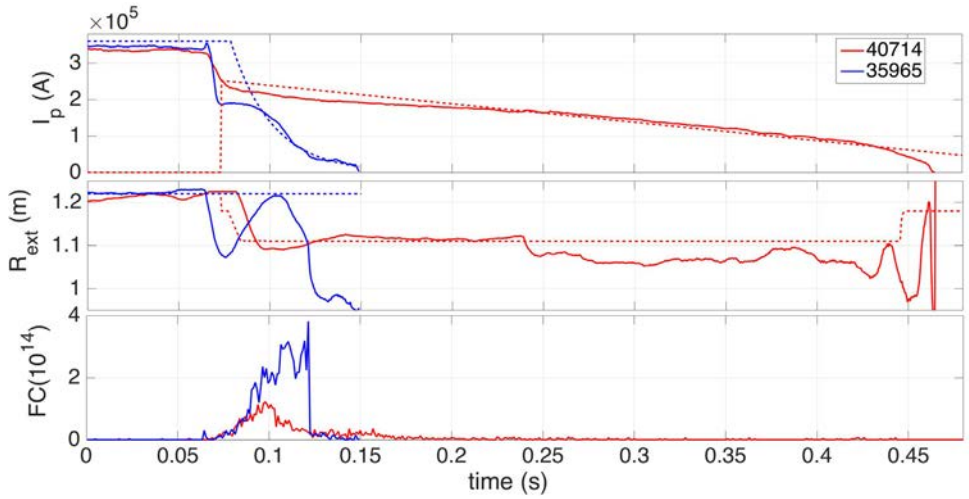

Figure 3. Experimental test of the RE control algorithm. The RE beam current, the RE beam external radius ($I_{\rm p}$ and $R_{\rm ext}$ references are in dashed lines) and the signal from the 235U fission chamber are reported in the different panels. Control active for pulse #40714.

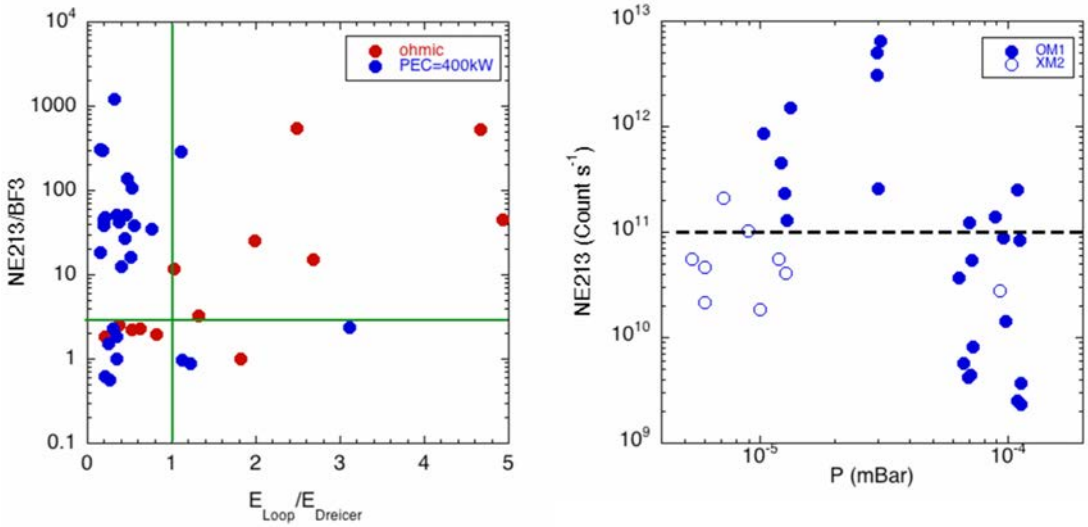

Figure 4. Left side: ratio between NE213 and BF3 signals as a function of toroidal electric field normalized to the Dreicer threshold for pure ohmic (red) and EC assisted (blue) pulses; the upper left region between the green lines identifies the conditions for RE presence below the Dreicer field threshold. Right side: signal from the liquid organic scintillator as a function of pre-filling pressure; below 10^{11} counts (black dashed line) no RE presence can be assumed (solid symbols are for OM1 wave polarization and open ones for XM2 wave).

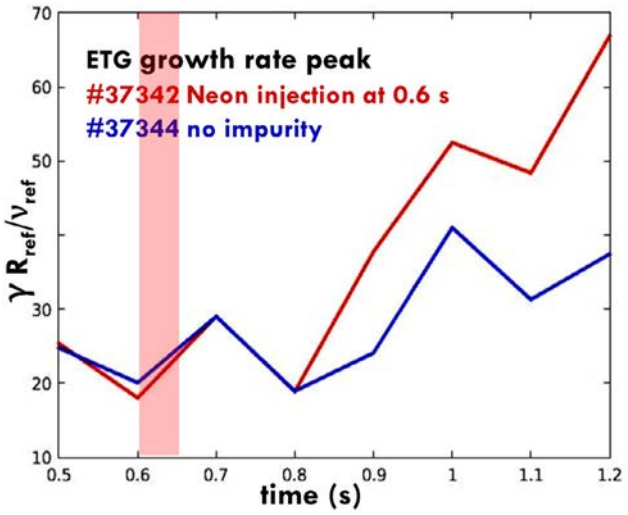

Figure 5. Time traces of the ETG growth rate peaks at $r/a = 0.5$. The red vertical box highlights the neon injection period for the pulse # 37342 (the impurity takes 150 ms to reach and to penetrate plasma).

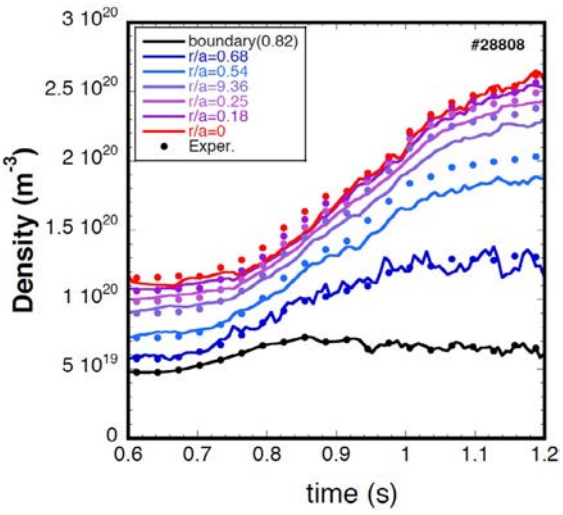

Figure 6. Density evolution at different normalized plasma radii for a pulse in the high density regime; simulated densities (lines) are well in agreement with experimental data (dots).

3. Transport studies

3.1. Neon impurity injection

Seeding of neon impurity in FTU ohmic plasmas causes a spontaneous rise of line-averaged electron density up to a factor two (notwithstanding the absence of deuterium gas puffing) associated with a significant increase of the peaking factor [13]. A qualitative estimate from UV spectroscopy measurements indicates that the density behavior can not be attributed simply to the stripped electrons from the puffed impurity [14, 15], but a modification of particle transport should be invoked in order to explain the spontaneous rise and the higher peaking. In order to investigate the mechanisms leading to the observed density peaking, a detailed linear micro-stability analysis of a neon-doped pulse performed on FTU has been carried out with the gyro-kinetic code GKW. In particular, the analysis of the neon-doped pulse, performed with an impurity density profile reconstructed by means of an impurity transport code [15], has been compared with the analysis of a similar un-doped pulse at the same line-averaged electron density and plasma parameters (toroidal magnetic field, plasma current). The doped pulse has higher ion and electron temperature gradients after the neon injection than the un-doped one; consequently, ITG and ETG modes turn out to be unstable, with higher values of the growth rates with respect to the similar un-doped pulse (figure 5). Finally, the fluxes analysis shows that ETG modes drive an inward flux for all the species and everywhere, so that the sharp peaking of the density profile could be due to the inward pinch brought about by ETG modes [16].

3.2. Thermo-diffusion in particle transport

In the high density regime, a sensible density peaking is observed, subsequent the formation of a strong MARFE thermal instability [17] at plasma edge. While central density is increasing by about a factor 2, edge chords, within a large plasma shell, remain almost unchanged, so that strong density gradients are generated between $r/a = 0.6$ and 0.8 [18]. The peaking of density profile is preceded by a drop of temperature in a wide peripheral region, caused by the thermal collapse at the edge which led to the MARFE formation. Having observed a good correlation between density and temperature characteristic lengths, a thermo-diffusive term given by:

$$\Gamma_p = -D_{\mathrm{T}} \frac{n_e}{T_e} \frac{\partial T_e}{\partial r} \tag{3}$$

with the coefficient D_{T} constant in time and space, has been taken into account in the diffusion equation to verify to which extent it can reproduce the effect on density profile. A neutral diffusion code has been used to estimate the contribution of neutrals to particle balance; according to these calculations, the source term remains negligible across most of the plasma section and in particular in the region where the changes of density gradient are observed. Therefore, simulations have been performed neglecting the source term in the diffusion equation. It is found that the increase of peaking can be explained with a sensible increase of the total inward particle pinch between $r/a = 0.5$ and 0.8, and the density profile evolution is well reproduced using a particle pinch term with dependence on temperature gradients, with the expression given by Γ_p and $D_{\mathrm{T}} = 0.05\,\mathrm{m^2\,s^{-1}}$. The simulated density evolution at different radii is shown together with experimental values in figure 6 for a given pulse [19].

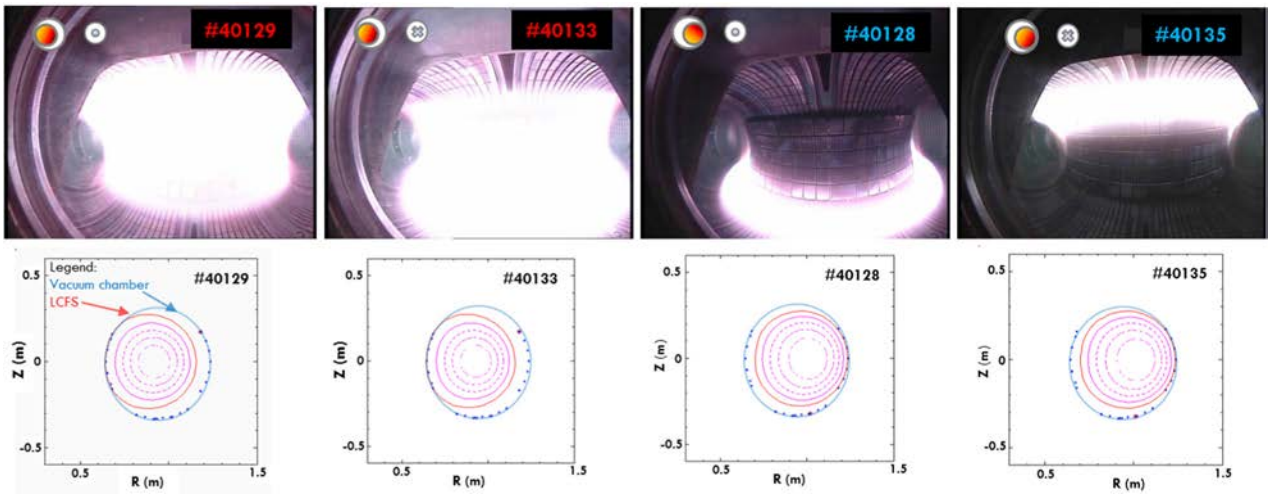

Figure 7. Visible camera images for the four different configurations performed to study the ion drift effects on MARFE. The plasma position and the magnetic field direction are shown by the insets (high magnetic field to the left). The flux maps are also reported in the bottom.

3.3. Ion drift effects on MARFE

A study of the ion drift effects (∇B and curvature drifts) on the MARFE instability has been performed by a specific experimental session on FTU, including some pulses with reversed toroidal magnetic field, and pushing the plasma column towards the internal side (high magnetic field) or external side (low magnetic field) of the vacuum chamber, respectively. The MARFE localization with respect to the ion drift direction has been compared for four different configurations (figure 7).

It is worth noting that the MARFE instability is localized at the high field side, where the heat flux from the core is lower, so that, for the two configurations with the plasma column pushed towards the external side of the vacuum chamber, the MARFE is detached from the internal toroidal limiter and the field sign provokes the stable MARFE positioning in the upper or lower mid-plane, in agreement with the direction of the ion drift velocity [20]:

$$\vec{v}_D = \frac{(v_\perp^2/2 + v_\parallel^2)}{\Omega R}\hat{R} \times \hat{B} \qquad (4)$$

where Ω is the gyro-frequency. On the other hand, the role of the ion drift has to be clarified when the MARFE is pushed towards the toroidal limiter and the interaction with the wall has to be considered.

4. High density regimes

4.1. Density limit scaling laws

Dedicated density limit experiments were performed on FTU in recent years, exploring the high density domain in a wide range of plasma current and toroidal magnetic field values [21]. New data were collected in the latest experimental campaigns, extending the study of the density limit towards lower values of toroidal magnetic field and plasma current. All pulses of the ultimate database were performed with a continuous gas flow injected into the plasma in order to produce a smoothly increasing density up to the disruption for density limit. The obtained results confirmed the edge nature of the density limit, as a Greenwald-like scaling was obtained for the maximum achievable line-averaged density along a peripheral chord with normalized radius $r/a = 0.8$ (figure 8, left side). Furthermore, a clear scaling of the maximum achievable line-averaged density along a central chord with the toroidal magnetic field only was found (figure 8, right side) and successfully interpreted as due to interplay between the Greenwald edge limit and the specific density profile behavior when approaching the density limit, with the density peaking linearly depending on the edge safety factor at the density limit [21].

4.2. MHD activity

Density limit disruptions are usually ascribed to a thermal instability occurring when the radiation loss near the edge region overcomes the heat flux emerging from the core. The ensuing contraction of the temperature profile leads to a shrinkage of the current profile driving unstable a global MHD mode, such as the tearing mode, leading to disruption if the density continues to grow (figure 9). Whereas this traditional explanation for the appearance of a low-order tearing mode (usually of poloidal mode number $m = 2$ and toroidal mode number $n = 1$) when the density increases towards the limit is correct, it has proved difficult to obtain a robust onset criterion based on the classical linear instability. The analysis of the linear stability of a 2/1 tearing mode in high density plasmas on FTU has been performed by means of a Δ' code in cylindrical geometry [22] and also by means of the complete linear resistive MHD code MARS, with the current density profile obtained from the JETTO transport code, considering the electron temperature profile from the ECE diagnostic and assuming Spitzer resistivity. Our study has highlighted a destabilization with increasing peaking of the current profile during the density ramp-up, in agreement with the experimental observations. In particular, a slight outward shift of the $q = 2$ surface during the density ramp-up has been observed, and the destabilization is associated with an increase of the local current density gradient.

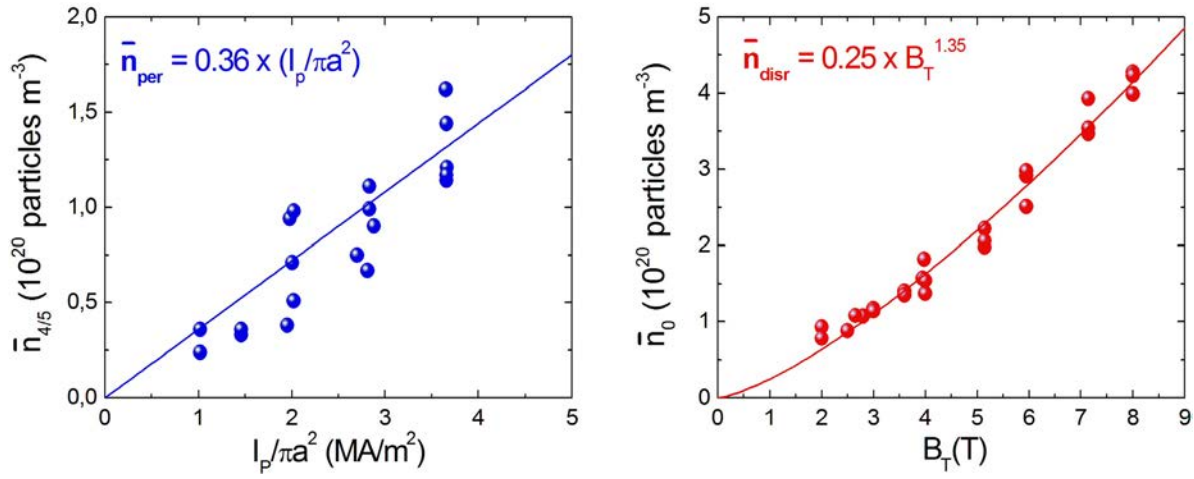

Figure 8. Left side: line-averaged density for a peripheral chord ($r/a = 4/5$) at the disruption versus the plasma current density. Right side: line-averaged density for a central chord ($r/a = 0$) at the density limit disruption versus the toroidal magnetic field.

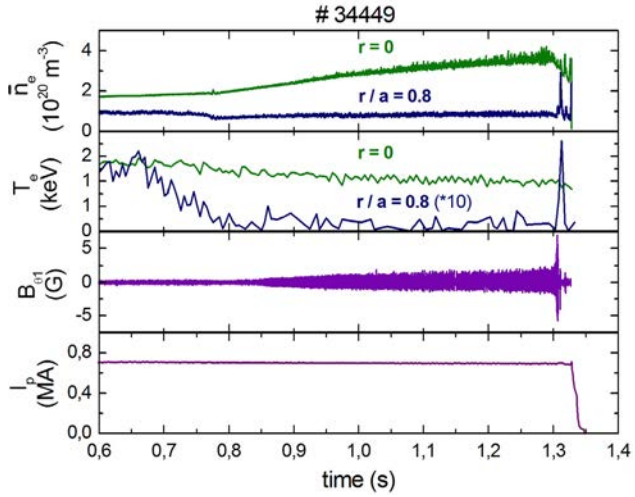

Figure 9. Time traces of some relevant quantities for the MHD activity in the high density regime on FTU: central and peripheral line-averaged density, central and peripheral electron temperature, poloidal magnetic perturbation, plasma current.

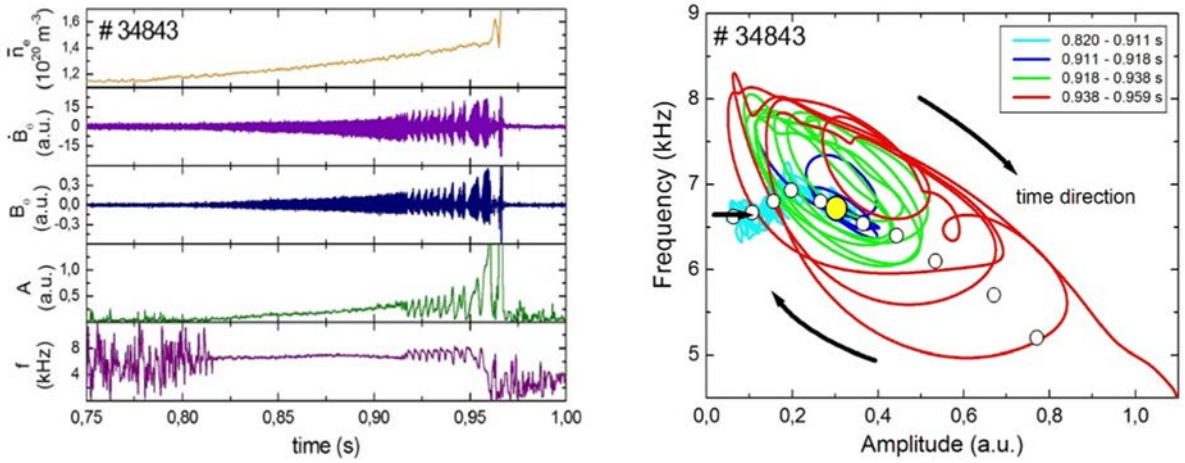

Figure 10. Left side: time traces of some relevant quantities for the MHD activity in a high density pulse (central line-averaged density, output from the pick-up coil, poloidal magnetic perturbation, mode amplitude, mode frequency). Right side: mode evolution on the amplitude/frequency plane; the evolution of amplitude and frequency envelopes is also reported as open circles (the yellow corresponds to the critical mode amplitude for transition from smooth to cyclic behavior).

Concerning the development of the tearing modes during the pre-programmed plasma density ramp-up up to the density limit on FTU, it is worth noting that the evolution of the magnetic islands shows a complex behavior which is not observed in the low density regime. In the first phase, the magnetic island grows smoothly at constant rotation frequency. Afterward, amplitude and frequency feature oscillations with larger and larger excursion. Finally, the island grows quickly to large amplitude and locks: this stage ends in a disruption (figure 10, left side). By contrast, large amplitude tearing modes in low density pulses feature smooth frequency roll-over until locking, at nearly constant island amplitude. The amplitude and frequency oscillations in high density pulses show a well defined phase portrait [23], determining a so-called 'limit cycle' on the amplitude/frequency plane (figure 10, right side). The existence of a stage with large amplitude and frequency modulations does not seem to be caused by interaction between modes of different helicity, the 2/1 tearing mode being the only large amplitude one in our pulses. On the other hand, the amplitude and frequency modulations could be caused by island self-healing phenomena, with a recursive island fragmentation mechanism, as supported by the observation of spatial harmonics (i.e. 4/2 and 6/3 components) that grow and strongly distort the island shape before each amplitude drop. Numerical simulations by a 4-field code are in progress to elucidate the mechanism leading to island distortion and its relationship with the characteristics of high density regimes.

5. Plasma-facing components (PFC)

5.1. Liquid lithium limiter (LLL)

Research on liquid metals is pursued as a viable solution to solve the power exhaust problem. The experiments on FTU aim at testing a cooled liquid lithium limiter (CLL) and subsequently a cooled liquid tin limiter (TLL) under reactor relevant thermal loads up to 10 MW m^{-2} in stationary conditions. Until now, CLL experiments with heat loads higher than 2.3 MW m^{-2} and time duration longer than 1.5 s were prevented by the onset of some hot spots on the joint points of the strips of the capillary porous system structure. For this reason, a new CLL, with a larger curvature radius and a better control system for the temperature monitoring and the water circulation, has been realized and implemented for the next experimental campaign. However, the tests performed on the LLL in the latest experimental campaign are extremely encouraging, showing heat loads on the LLL up to 6 MW m^{-2}, as derived by means of the plasma edge parameters measured by Langmuir probes for pulses with $B_T = 4$ T and $I_p = 500$ kA, with no damage of the exposed surface (figure 11) [24]. In preparation of the next CLL experiments, the pulse duration for lower plasma currents ($I_p = 0.25 \div 0.35$ MA) has been extended up to 4.5 s ($B_T = 2.5 \div 4$ T), in order to test the limiter in stationary high heat flux conditions [25]. Furthermore, to maximize and control the heat load on limiters, elongated configurations (with the elongation k from 1.06 to 1.18) have been also obtained for 3.5 s, with the X-point just outside the plasma chamber [26].

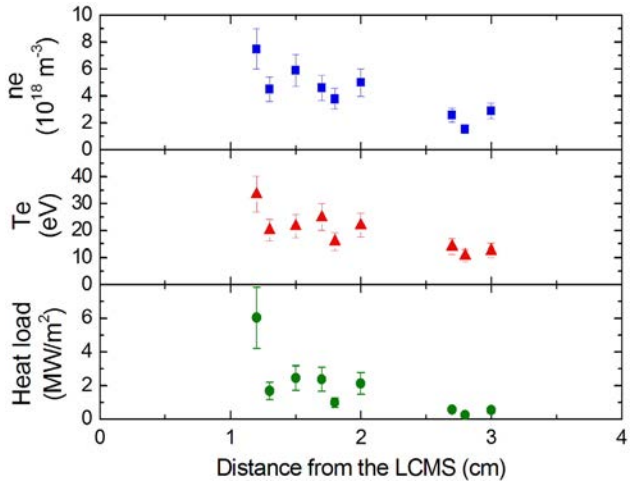

Figure 11. Electron density, electron temperature and averaged heat loads on LLL in stationary conditions for pulses with different distance from the last closed magnetic surface (LCMS).

5.2. Tungsten enrichment of surface layer

A P92 steel sample with low W concentration (about 1%) was exposed in the FTU scrape-off layer during steady state pulses, with the purpose of checking the effectiveness of preferential sputtering in the W enrichment of the very surface layer of first wall material, like EUROFER steel [27]. The latter could represent a valuable alternative to a solid W or W-coated first wall, with obvious economic advantages and decrease of weight. To avoid sample contamination by a nearby source of Fe, the sample holder was made of Ti. Plasma edge parameters were analyzed by Langmuir probes and ERO code simulation of Fe erosion were carried out for comparison with experimental erosion. After exposure, the sample was analyzed in collaboration with the National Institute for Laser, Plasma and Radiation Physiscs of Romania and the Ruder Boskovic Institute of Croatia. Rutherford back-scattering spectrometry (RBS) analysis of the exposed sample shows, with respect to a non-exposed one, a surface enrichment of both W and Mo, the latter probably coming also from the TZM toroidal limiter and/or the Mo outer poloidal limiter (figure 12).

5.3. Dust studies

Dust from FTU has been collected and analyzed and it was found that the metallic population exhibits a high fraction (up to 70 wt%) of magnetic grains. Neutron and x-ray diffraction analysis on crystalline structures of that dust have thrown new light on the mechanism of formation of ferromagnetic dust in tokamaks. The origin of ferromagnetic dust is related to changes of the crystalline phase of iron from non magnetic to magnetic phase in molten drops ejected by austenitic stainless steel (non-magnetic) PFC, such as first walls, diagnostics, antennas, etc. Two mechanisms are believed to be responsible for this change of phase; the first is the effect of a strong magnetic field environment during the re-solidification of molten grains; the second is the stabilization of ferrite phase during the re-solidification of molten stainless steel grains due to the strong temperature quenching as soon as the molten grains get in contact with the

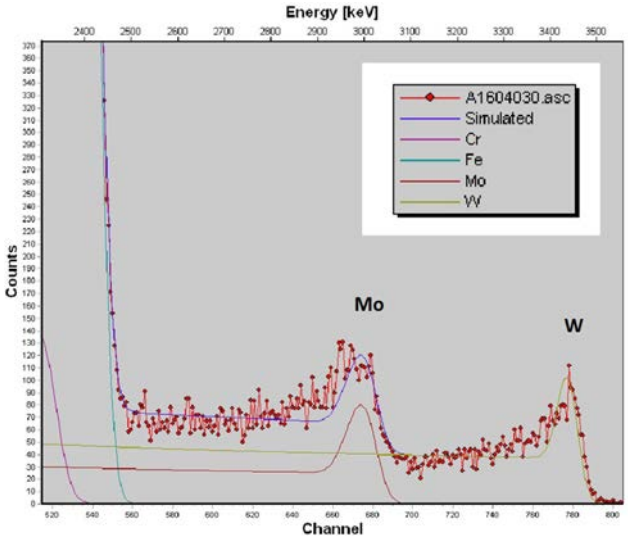

Figure 12. RBS spectrum of P92 sample showing the W and Mo surface enrichment.

cryogenic walls of FTU. The presence of ferromagnetic particles in tokamaks could pose new problems due to their interaction with the magnetic field; in fact magnetic grains could be lifted-up during the ramping-up phase of the magnetic field due to ∇B force, and interfere with the start-up phase of plasma pulse [28].

6. Diagnostics

6.1. RE imaging and spectrometry

A specific activity was focused on the design, development and construction of the prototype of a portable runaway electron imaging spectroscopy (REIS) system for use in medium size tokamaks, e.g. AUG. The system permits the simultaneous detection of forward and backward image and VIS/NIR spectra of synchrotron radiation from in-flight RE. This data will permit to obtain information on the RE energy distribution function in the various phases of a plasma pulse, particularly during runaway plateaus following disruption events. The new diagnostic is based on a wide-angle visible camera and an incoherent bundle of optical fibers coupled to 2 visible light spectrometers and 1 near-infrared spectrometer. The prototype was tested in FTU during the 2015 experimental campaign in several runaway pulses at 4 T and 5 T (figure 13), obtaining useful spectra in the visible 350–850 nm and infrared 900–2100 nm range [3]. Forward and backward RE synchrotron emission was measured, and a clear distinction was observed between the two cases, with the backward emission negligible with respect to the forward one, as shown by the upper frames of figure 13. The calibration of the infrared spectrum and the data interpretation are on going.

6.2. Fast infrared camera

The relevance of the thermal load measurements during disruptions in a limiter machine relies on the evidence that in a divertor tokamak the plasma configuration degrades to L-mode before the thermal quench. In FTU the plasma

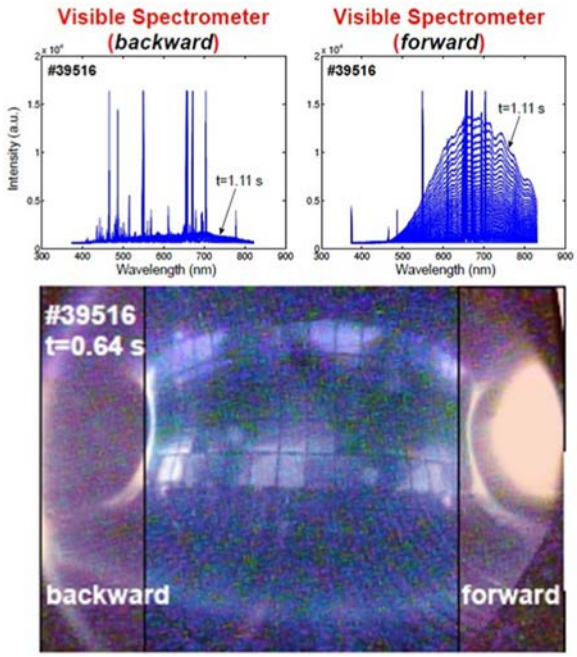

Figure 13. Visible camera image and visible spectra (raw data) for a runaway pulse in FTU (the visible spectra show also the impurity spectral lines).

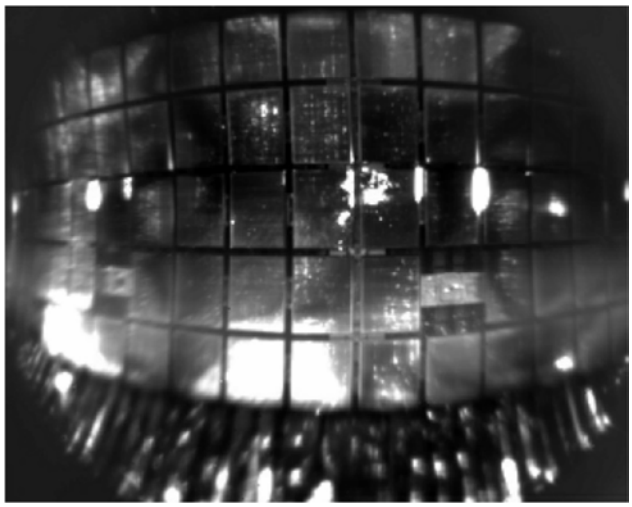

Figure 14. Post-disruption infrared image of a toroidal limiter sector.

column usually leans on the inboard toroidal limiter and during the current-quench it is pushed further inwards: therefore the largest heat load is expected to occur on the toroidal limiter. The thermo-graphic analysis of the inboard toroidal limiter has been recently carried out, by means of an optical system consisted of 14 Germanium lenses and able to transfer the image of one of the 12 toroidal limiter sectors, through the port, to an infrared camera. Several disruptions have been monitored, providing the pattern of limiter heating by disruption heat loads and the quantitative analysis of the data is in progress (figure 14). Complementary to the measurement of thermal load on the toroidal limiter is also the detection of frequent and massive presence, during disruption, of eroded or mobilized dust. Its survival in the vacuum chamber for a long

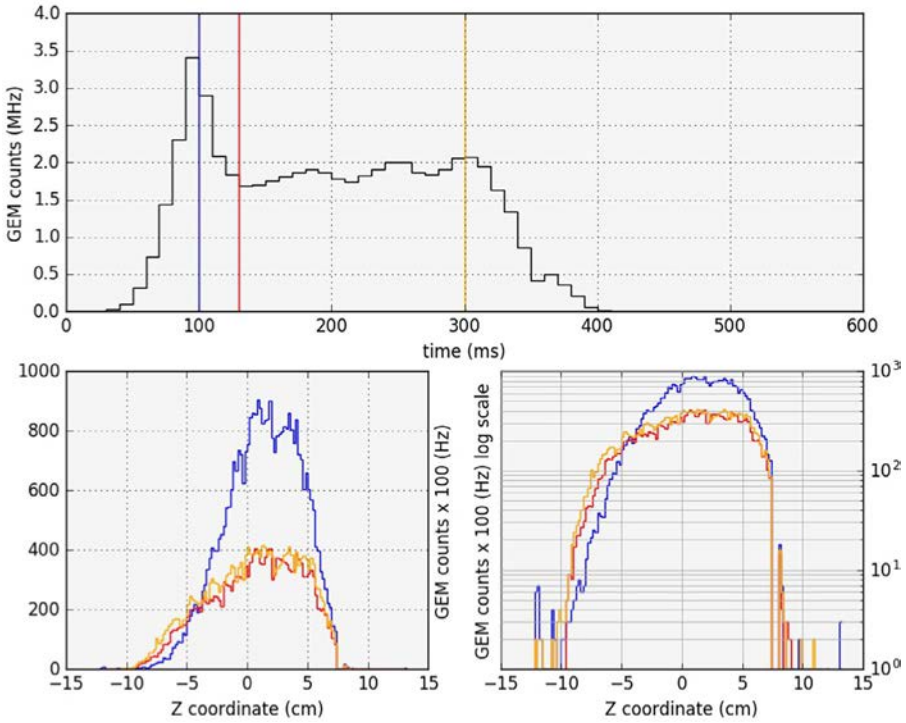

Figure 15. Top: temporal trace as measured from the GEM detector, obtained summing on all the pad counts. Bottom: plasma profiles measured by the GEM detector at different times. Pulse # 40613.

time after the disruption confirms the indirect detection carried out in the past with Thomson scattering diagnostic [29].

6.3. Triple-GEM detector

The use of triple-GEM (gas electron multiplier [30]) detectors for soft x-ray diagnostics on tokamak plasmas has been successfully demonstrated by recent applications on KSTAR [31, 32]. A similar detector has been recently tested on FTU. The detector is equipped with a read-out anode having 128 pads distributed along a vertical line. Each pad has an area of 500×500 μm^2 (with a pitch of 700 μm) and a field of view of 1.4×1.4 mm^2 on the plasma, according to the realized geometrical configuration. The GEM detector uses a flowing $ArCO_2$ gas mixture at atmospheric pressure and it works in counting mode: charge released in the drift gap moves towards the GEM foils where it is proportionally amplified; then a current pulse is induced on pads and this is counted as one when a threshold level is exceeded. The soft x-ray emission between 2 and 15 keV for FTU pulses is detected with a frame rate of 100 Hz and the temporal trace and the plasma profiles can be reconstructed, as shown in figure 15 for a pulse with $B_T = 2.7$ T and $I_p = 350$ kA. The plasma profiles are shown also on semi-logarithmic scale, from which it can be observed the very high dynamic range of the GEM detector: it can go from the single photon to 10^3 photons. Two GEM cameras (with vertical and horizontal orientation) will be installed in the future on FTU, in order to realize a more performing tomography system with respect to the conventional diode system, actually working on FTU.

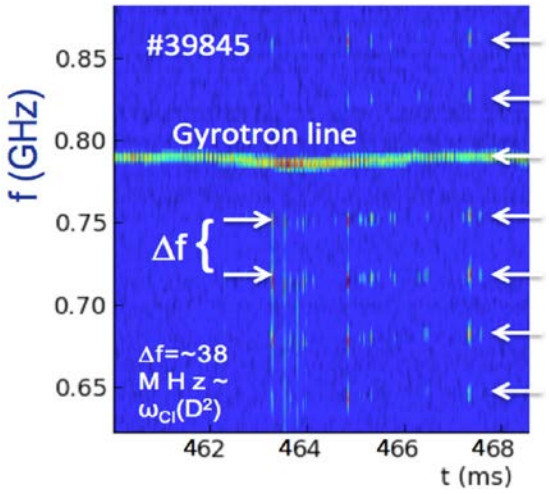

Figure 16. Asynchronous sequence of bursts emitted at frequency multiple of the deuteron ion cyclotron frequency both above and below the gyrotron line.

6.4. Collective Thomson scattering (CTS)

The investigation on possible excitation of parametric decay instabilities by EC beams in presence of magnetic islands using the CTS diagnostic has been recently performed on FTU, launching a gyrotron probe beam (140 GHz, 400 kW) and receiving the CTS beam in symmetric and asymmetric configurations with respect to the equatorial plane, in different conditions of plasma density and magnetic field (with or without the EC resonance in the plasma), and with magnetic islands generated by neon

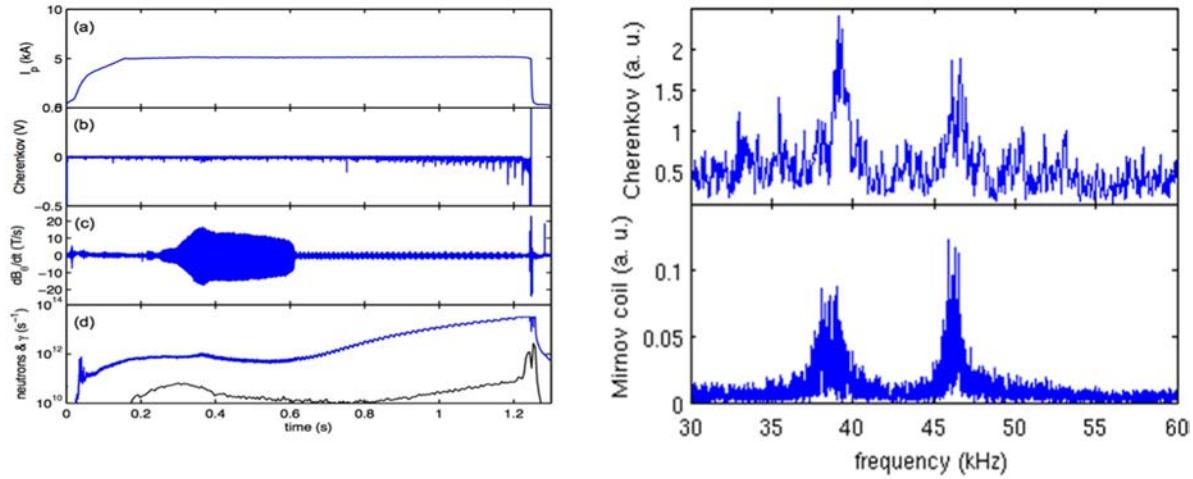

Figure 17. Scenario involving island quasi-locking and BAE excitation ($B_T = 6$ T, $I_p = 0.5$ MA). Pulse # 37655. Left side: plasma current *(a)*, Cherenkov signal *(b)*, Mirnov coils *(c)*, NE213 and BF3 (black line) signals *(d)*. Right side: power spectral density in the high frequency range ($30 \div 60$ kHz) of (bottom) Mirnov and (top) Cherenkov signals.

injection. The CTS diagnostic was renewed [33, 34] with the acquisition of a fast digitizer, which allowed the observation of a number of spectral features with very high time and frequency resolution. Two of them are presently under deeper investigation [35]. The first is a rapid asynchronous sequence of bursts detected at frequency multiples of the (deuterium) ion cyclotron frequency above and below the gyrotron frequency (figure 16), occurring in connection with an MHD activity leading to plasma disruption. The second is a periodic emission at frequency around 15 MHz from the probe frequency. The correlation of the observed peaks of this emission with the transit of the island O-point inferred from magnetic probes signals is being investigated, to characterize the observations and exclude parasitic effects, as well as breakdown phenomena in front of the antennas. Further improvements of the frequency band and the addition of a second radiometer recently integrated in the CTS system [36] will allow a clearer interpretation of the signals.

6.5. Cherenkov probe

An optical diagnostic system based on the Cherenkov effect was recently installed on FTU, demonstrating a high level of detail in detecting RE losses driven by magnetic islands [37]. The Cherenkov probe was tested in various plasma scenarios, including experiments where the plasma density is intentionally reduced until REs are observed (figure 17, left side). In the initial phase of such low density pulses, a tearing mode instability involving a rotating island develops and the Cherenkov signal maxima occur when the island O-point faces the probe, demonstrating that REs are expelled in the interaction with the magnetic perturbation due to the island. On the other hand, in the final quasi-locking stage, when the island rotates at some tens of Hz and the magnetic signal is dominated by the high-frequency BAE [38] component (figure 17, right side), the Cherenkov signal presents a bursty emission modulated by the island rotation frequency, indicating that RE losses promptly respond to island amplitude fluctuations. This is the first time BAEs have been detected using a non-magnetic plasma diagnostics.

The main limitation of the present Cherenkov probe is that it does not provide information on the spatial and energy distribution of incoming electrons. A system upgrade that will enable energy and spatially resolved analysis of RE losses in FTU has been prepared for the next experimental campaign, to evaluate the potential of this diagnostic system for implementation in fusion reactors.

7. Conclusions

Experiments on runaway electrons have confirmed a new threshold for the critical electric field calculated including synchrotron radiation losses and the possibility to control the position and the current of post-disruption runaway beam acting on the central solenoid, and they have highlighted the presence of runaway electrons also below the expected electric field threshold in experiments of EC assisted plasma start-up.

Transport studies have been performed to investigate the mechanisms leading to the observed density peaking in neon-doped pulses and in the high density regime, where the density profile evolution has been well reproduced using a thermo-diffusive pinch term in the particle transport equation; in addition, the ion drift effects on the MARFE instability have been investigated by a specific experimental session.

Dedicated density limit experiments have confirmed the edge nature of the density limit, and the analysis of the linear stability of the 2/1 tearing mode observed in high density plasmas has highlighted a destabilization with increasing peaking of the current profile during the density ramp-up, while the final phase of the mode temporal evolution is characterized by limit cycles on the amplitude/frequency plane.

Concerning the studies about the plasma-facing components, a liquid lithium limiter has been tested, showing heat

loads up to 6 MW m^{-2} with no damage of the exposed surface, a P92 steel sample has been exposed in the scrape-off layer, confirming a W enrichment of the surface layer, and dust has been collected and analyzed, exhibiting a high fraction of magnetic grains.

New diagnostics, such as a visible/infrared detector for in-flight runaway studies, a fast infrared camera for thermographic analysis and a triple-GEM detector for soft x-ray diagnostics, have been successfully installed and tested, and new capabilities of the collective Thomson scattering diagnostic and of the Cherenkov probe have been explored.

Acknowledgments

This work has been carried out within the framework of the EUROfusion Consortium and has received funding from the Euratom research and training programme 2014-2018 under grant agreement No 633053. The views and opinions expressed herein do not necessarily reflect those of the European Commission.

References

[1] Gormezano C. *et al* 2004 *Fusion Sci. Technol.* **45** 297
[2] Popovic Z. *et al* 2016 *Phys. Plasmas* **23** 122501
[3] Esposito B. *et al* 2017 *Plasma Phys. Control. Fusion* **59** 014044
[4] Connor J.W. and Hastie R.J. 1975 *Nucl. Fusion* **15** 415
[5] Rosenbluth M.N. and Putvinski S.V. 1997 *Nucl. Fusion* **37** 1355
[6] Martin-Solis J.R. *et al* 2010 *Phys. Rev. Lett.* **105** 185002
[7] Carnevale D. *et al* 2015 *Proc. 42nd EPS Conf. on Plasma Phys. (Lisbon, Portugal, 22–26 June 2015)* vol 39E (ECA) P4.192 (http://ocs.ciemat.es/EPS2015PAP/pdf/P4.192.pdf)
[8] Hollmann E.M. *et al* 2013 *Nucl. Fusion* **53** 083004
[9] Saint-Laurent F. *et al* 2013 *Fusion Sci. Technol.* **64** 711
[10] Carnevale D. *et al* 2016 Analysis of runaway beam suppression experiments in FTU *Preprint: 2016 IAEA Fusion Energy Conf. (Kyoto, Japan, 17–22 October 2016)* EX/P8-22 (https://nucleus.iaea.org/sites/fusionportal/Shared%20Documents/FEC%202016/fec2016-preprints/preprint0527.pdf)
[11] Granucci G. *et al* 2011 *Nucl. Fusion* **51** 073042
[12] Granucci G. *et al* 2015 *Nucl. Fusion* **55** 093025
[13] Mazzotta C. *et al* 2015 *Nucl. Fusion* **55** 073027
[14] Mazzotta C. *et al* 2013 *Proc. 40th EPS Conf. on Plasma Phys. (Espoo, Finland, 1–5 July 2013)* vol 37D (ECA) P4.140 (http://ocs.ciemat.es/EPS2013PAP/pdf/P4.140.pdf)
[15] Mazzotta C. *et al* 2015 *Proc. 42nd EPS Conf. on Plasma Phys. (Lisbon, Portugal, 22–26 June 2015)* vol 39E (ECA) P4.114 (http://ocs.ciemat.es/EPS2015PAP/pdf/P4.114.pdf)
[16] Mazzotta C. *et al* 2016 *Proc. 43rd EPS Conf. on Plasma Phys. (Leuven, Belgium, 4–8 July 2016)* vol 40A (ECA) P5.019 (http://ocs.ciemat.es/EPS2016PAP/pdf/P5.019.pdf)
[17] Lipschultz B. 1987 *J. Nucl. Mater.* **145** 15
[18] Tudisco O. *et al* 2010 *Fusion Eng. Des.* **85** 902
[19] Tudisco O. *et al* 2016 Evidence of thermo-diffusive pinch in particle transport *Preprint: 2016 IAEA Fusion Energy Conf. (Kyoto, Japan, 17–22 October 2016)* EX/P8-24 (https://nucleus.iaea.org/sites/fusionportal/Shared%20Documents/FEC%202016/fec2016-preprints/preprint0279.pdf)
[20] Mazzotta C. *et al* 2016 Dynamic and frequency behaviour of the MARFE instability on FTU *Proc. 22nd PSI Conf. (Rome, Italy, 30 May–3 June 2016)* P4.42; *Nucl. Mater. Energy* at press (https://dx.doi.org/10.1016/j.nme.2017.02.008)
[21] Pucella G. *et al* 2013 *Nucl. Fusion* **53** 083002
[22] Pucella G. *et al* 2013 *Proc. 40th EPS Conf. on Plasma Phys. (Espoo, Finland, 1–5 July 2013)* Vol. 37D (ECA) P5.139 (http://ocs.ciemat.es/EPS2013PAP/pdf/P5.139.pdf)
[23] Pucella G. *et al* 2015 *Proc. 42nd EPS Conf. on Plasma Phys. (Lisbon, Portugal, 22–26 June 2015)* vol 39E (ECA) P4.112 (http://ocs.ciemat.es/EPS2015PAP/pdf/P4.112.pdf)
[24] Stangeby P.C. and McCracken G.M. 1990 *Nucl. Fusion* **30** 1225
[25] Mazzitelli G. *et al* 2016 Liquid metals experiments on FTU *Preprint: 2016 IAEA Fusion Energy Conf. (Kyoto, Japan, 17–22 October 2016)* EX/P8-21 (https://nucleus.iaea.org/sites/fusionportal/Shared%20Documents/FEC%202016/fec2016-preprints/preprint0224.pdf)
[26] Reimerdes H. *et al* 2014 *Proc. 42nd EPS Conf. on Plasma Phys. (Lisbon, Portugal, 22–26 June 2015)* vol 39E (ECA) P4.117 (http://ocs.ciemat.es/EPS2015PAP/pdf/P4.117.pdf)
[27] Roth J. *et al* 2014 *J. Nucl. Mater.* **454** 1
[28] De Angeli M. *et al* 2015 *Nucl. Fusion* **55** 123005
[29] Giovannozzi E. *et al* 2006 *Proc. 33rd EPS Conf. on Plasma Phys. (Rome, Italy, 19–23 June 2006)* vol 30I (ECA) P2.093 (http://epsppd.epfl.ch/Roma/pdf/P2_093.pdf)
[30] Sauli F. 1997 *Nucl. Instrum. Methods* A **386** 531
[31] Pacella D. *et al* 2013 *Nucl. Instrum. Methods* A **720** 53
[32] Pacella D. *et al* 2013 *Proc. 40th EPS Conf. on Plasma Phys. (Espoo, Finland, 1–5 July 2013)* vol 37D (ECA) P5.118 (http://ocs.ciemat.es/EPS2013PAP/pdf/P5.118.pdf)
[33] Bin W. *et al* 2015 *Fusion Eng. Des.* **96-97** 733
[34] Bin W. *et al* 2015 *J. Instrum.* **10** P10007
[35] Bruschi A. *et al* 2016 Observation of short time-scale spectral emissions at millimeter wavelengths with the new CTS diagnostic on the FTU tokamak *Preprint: 2016 IAEA Fusion Energy Conf. (Kyoto, Japan, 17–22 October 2016)* EX/P8-23 (https://nucleus.iaea.org/sites/fusionportal/Shared%20Documents/FEC%202016/fec2016-preprints/preprint0275.pdf)
[36] Bin W. *et al* 2016 *Rev. Sci. Instrum.* **87** 11E507
[37] Causa F. *et al* 2015 *Nucl. Fusion* **55** 123021
[38] Buratti P. *et al* 2005 *Nucl. Fusion* **45** 1446